

See discussions, stats, and author profiles for this publication at: <https://www.researchgate.net/publication/359450195>

# Geomechanical model construction to resolve field stress profile and reservoir rock properties of Jurassic Hugin Formation, Volve field, North Sea

Article in Geomechanics and Geophysics for Geo-Energy and Geo-Resources · April 2022

DOI: 10.1007/s40948-022-00359-5

---

CITATIONS

3

READS

625

4 authors, including:



Sankhajit Saha

Indian Institute of Technology Bombay

13 PUBLICATIONS 8 CITATIONS

[SEE PROFILE](#)



Vikram Vishal

Indian Institute of Technology Bombay

117 PUBLICATIONS 3,364 CITATIONS

[SEE PROFILE](#)



Bankim Mahanta

Indian Institute of Technology Bhubaneswar

23 PUBLICATIONS 911 CITATIONS

[SEE PROFILE](#)



# Geomechanical model construction to resolve field stress profile and reservoir rock properties of Jurassic Hugin Formation, Volve field, North Sea

Sankhajit Saha · Vikram Vishal · Bankim Mahanta · Sarada Prasad Pradhan

Received: 2 June 2021 / Accepted: 2 January 2022

© The Author(s), under exclusive licence to Springer Nature Switzerland AG 2022

**Abstract** Geomechanical characterisation of a hydrocarbon reservoir has multifold implications throughout the lifecycle of an oil and gas field, starting from exploration through development to abandon stage. At each phase, geomechanics, its related challenges and complications are different, and thus the perspective of the solution. To provide a practical and reasonable answer, it is imperative to have a robust well based 1D geomechanical model in the first place. This work made an effort to construct a geomechanical model based on well log data, geological information, and drilling-related events in the Hugin Formation of the Volve field in the central part of the North Sea basin. The geomechanical model indicates a strike-slip fault regime ( $S_{H\max} > S_v > S_{h\min}$ ) in the

reservoir section. Vertical stress ( $S_v$ ) gradient was estimated at 17 ppg (~77 MPa) in the reservoir section. Pore pressure profile shows variation along the stratigraphic sequence, and the maximum pressure gradient appeared was approximately 11–11.66 ppg (~30–34 MPa) in Skade Formation and 9.61 ppg (~33–36 MPa) in Hugin Formation. Within the reservoir intervals, uniaxial compressive strength ranges around 33–39 MPa, Young's modulus ( $E$ ) at 15–18 GPa, Poisson's ratio ( $\nu$ ) at 0.2–0.4 and internal friction at around 0.6 are observed. Based on previous references, the net maximum horizontal stress orientation appears to be approximately E–W. The study indicates mud weight used in Hugin Formation to drill is more than sufficient for wellbore stability. Mud weight estimation for various well trajectories was also analysed. The proposed base model for Hugin Formation of theta vest structure shall help plan future field development strategies and feasibility considerations for possible CO<sub>2</sub> sequestration.

---

S. Saha · V. Vishal (✉)  
Computational and Experimental Geomechanics  
Laboratory, Department of Earth Sciences, Indian Institute of Technology Bombay, Mumbai 400076, India  
e-mail: v.vishal@iitb.ac.in

S. Saha  
Reservoir Technical Service, Baker Hughes,  
Mumbai 400708, India

B. Mahanta  
Department of Geology, Central University of Tamil Nadu,  
Thiruvarur, Tamil Nadu 610005, India

S. P. Pradhan  
Department of Earth Sciences, Indian Institute of Technology Roorkee, Roorkee, Uttarakhand 247667,  
India

## Article highlights

- An investigation has been performed to understand the geomechanical properties and optimum orientation of drilling in the Hugin Formation.
- Pore pressure data calibrated with direct pressure measurement, and the gradient shows higher than hydrostatic pressure, ~9.61 ppg.
- The stress state indicates a strong strike-slip fault regime within the Hugin Formation.

- Rock mechanical properties were calibrated with available core test data, and UCS values range from 31–41 MPa.

**Keywords** 1D geomechanical model · Strike-slip fault · Stress state · Wellbore stability · North Sea · Carbon sequestration

## 1 Introduction

Pore pressure and wellbore stability analysis are inevitable, considering their importance in the pre-drilling and post-drilling process and their applicability in exploration and reservoir development (Baouche et al. 2020). The state of stress in a hydrocarbon reservoir has significant implications throughout the lifecycle of a hydrocarbon field. At each phase, challenges are different, thus the solution. One of the common challenges is wellbore stability and overpressure during drilling. The statistical study conducted in the deep-water settings (water depth > 3000 ft) in the Gulf of Mexico indicates limited insight associated with pore pressure and wellbore instability took 5.6% of drilling time in non-subsalt wells and 12.6% of drilling time in the subsalt wells (York et al. 2009; Zhang 2011) which increased the non-productive time of wells. Zoback (2007) demonstrated a comprehensive geomechanical modelling workflow and various case studies related to geomechanical complications. Azim et al. (2011) showed 1D geomechanical workflow and addressed wellbore stability-related challenges associated with drilling in the Zubair shale/sand sequence of Kuwait from the Middle East and provided the solution. Incorporating well log and core data, Zoback (2007) illustrated 1D model workflows crucial for understanding geomechanical parameters. During drilling, trailing pore pressure and failures associated with wellbores are the most critical challenges that often lead to substantial non-productive times (NPT) and often lead to well abandonment. Borehole-wall stability is very much dependent on the pore pressure distributions, which is collectively dependent on various geological processes, rock mechanical and petrophysical properties. Within the limit of the target depth, it is always a good practice to maintain the mud pressure above the pore pressure and below the fracture pressure to maintain the safe drilling option

(Baouche et al. 2020). The geomechanical model plays a significant role in the subsurface CO<sub>2</sub> sequestration. As the pressure and stress fields get altered due to CO<sub>2</sub> injection, understanding in situ stress conditions and rock mechanical properties are essential (Shukla et al. 2010; Vishal 2017a, b; Vishal et al. 2018, 2015, 2013a, b). Altmann et al. (2010) reported the variation of horizontal stress with pore pressure and associated stress path. In the Otway Basin Pilot Project (OBPP), the geomechanical investigation was carried out for caprock integrity and fault reactivation due to CO<sub>2</sub> sequestration in the saline aquifer in the Naylor field (Shukla et al. 2010). In the Sleipner area of the North Sea, a CO<sub>2</sub> injection project has been conducted in Utsira Formation, a relatively shallow saline aquifer. It is the world's longest-running CO<sub>2</sub> injection project where geomechanical characterisation helped analyse the possible risks associated with CO<sub>2</sub> injection (Chadwick and Eiken 2013). In addition to several successful projects of CO<sub>2</sub> sequestration in shallow aquifers, a wide distribution of such formations with high CO<sub>2</sub> storage potential around the globe has been estimated (Chamwudhiprecha and Blunt 2012; Gale 2004; Nicot 2008).

The present study is focused on the Volvo field, North Sea. Many researchers have done several works in the North Sea fields due to their structural and geological complexity and associated challenges. Wiprut (2001) addressed stress field, wellbore stability and fault reactivation potential in Visund field, west of the Viking graben in the North Sea, which gave a broad picture of the geomechanical characteristics of Visund field and surrounding area. The world stress map is an excellent reference to understand horizontal stress azimuth ( $S_{H\max}$ ) (Zoback and Zoback 1989). Heidbach et al. (2018, 2010) showed the global stress pattern based on geophysical information; well log data, core data, etc., which further provided a ranking system based on data quality. Zoback (2007) also elaborated  $S_{H\max}$  orientation analysis procedure based on well log data, earthquake focal mechanism and structural pattern. Fang and Khaksar (2012) highlighted geomechanical issues and solutions related to CO<sub>2</sub> sequestration in a depleted reservoir from the Southern North Sea. A complete well-based geomechanical model had been established before carrying out the feasibility study by Fang and Khaksar (2012). They also highlighted the risks associated with drilling, and suggested possible solutions, however, field

and formation information were not clearly mentioned. Hillis and Nelson (2005) showed geomechanical implications such as fracture reactivation, wellbore stability, water flooding, and stress sensitivity for the Northern and Central North Sea. They employed generalised stress data for the Northern and Central North Sea up to 3 km depth.

While the above-mentioned studies show a broadly generalised understanding of stress state at the regional level, the present research primarily focuses on a single producing reservoir formation. This paper aims to understand the in-situ stress state and rock mechanical properties of Hugin formation in the Theta Vest structure of the Volve field in the North Sea based on the published database by Equinor. Also, we have tried to understand the optimum mud weight range for different well trajectories in the reservoir section.

Whenever log data are absent, a continuous pressure profile has been established based on drill events such as inflow, trip-gas, connection gas, tight hole, stuck events, pack off etc., for shallow section. Actual formation pressure data were used to ascertain the pore pressure within the reservoir section. Rock mechanical analysis had only been focused on the reservoir section. Seismic velocity-based pseudo density data and density log were considered for the vertical stress ( $S_v$ ) profile. Minimum horizontal stress ( $S_{h\min}$ ) was estimated based on the effective stress ratio (ESR) concept and calibrated with leak-off test (LOT) data. Fault frictional theory was implemented to constrain the maximum horizontal stress ( $S_{H\max}$ ) magnitude (Zoback 2007). World Stress Map and regional structural trend helped establish the  $S_{H\max}$  azimuth as no breakouts in image log, or multi-arm caliper data were available in the vertical wellbore (Heidbach et al. 2010; Zoback and Zoback 1989). In this paper oil field industry English unit is readily used to present the data. Pressure and stress values are presented in equivalent mud weight terms as ppg (pounds per gallon) unit. However, absolute values of rock strength, stresses and pore pressure are presented in the SI unit. Furthermore, in this manuscript, wherever it is required, we have provided both the units.

## 2 Geological settings of the area

The current study focuses on the Volve oilfield located eight kilometres north of the Sleipner Øst structure in the central part of the North Sea. The Theta vest structure in Volve oilfield is located between the Loke structure at East and Northwestern extension of Sleipner Øst structure. Figure 1 illustrates the map of the North Sea offshore and the location of the hydrocarbon producing Volve oilfield. The average water depth of the area is 84 m. Predominantly, the reservoir contains oil in Jurassic sandstones in the Hugin Formation combined stratigraphic and structural trap. The stratigraphic sequence was mapped from the Norland group to the crystalline basement based on 3D seismic interpretation and well log correlation. Theta vest structure appears to be domal in shape, underwent complex tectonic deformation in the past, and is located east of the main fault. The Sleipner area and South Viking graben suffered two major extensional events. The first extension phase occurred during the Permian to Triassic transition phase, where terrestrial sedimentation is predominant. During Triassic to Jurassic, the transition shifted from terrestrial to marginal to marine facies (Færseth 1996). Afterwards, during Middle Jurassic to Early Cretaceous, the 2nd phase of rifting occurred where deltaic to mouth bar deposits were predominant. Upper Triassic to Lower Jurassic formation is classified as an intra rift sequence. Several studies have been conducted to understand the direction of rifting during two phases of extension. Based on fault and fracture distribution patterns, it was concluded that the direction of spreading during both the rifting phases was primarily E–W (Osagiede et al. 2020).

Figure 2 depicts the generalised stratigraphic sequence with description of the lithology of South Viking graben and nearby areas. According to the report and data published by Equinor (Statoil 1993) the main reservoirs in the Theta vest area are Paleocene Heimdal Formation, Jurassic Hugin Formation and Triassic Skagerrak Formation. In this area, Heimdal Formation is water wet compared to the Sleipner Øst structure, which possesses significant

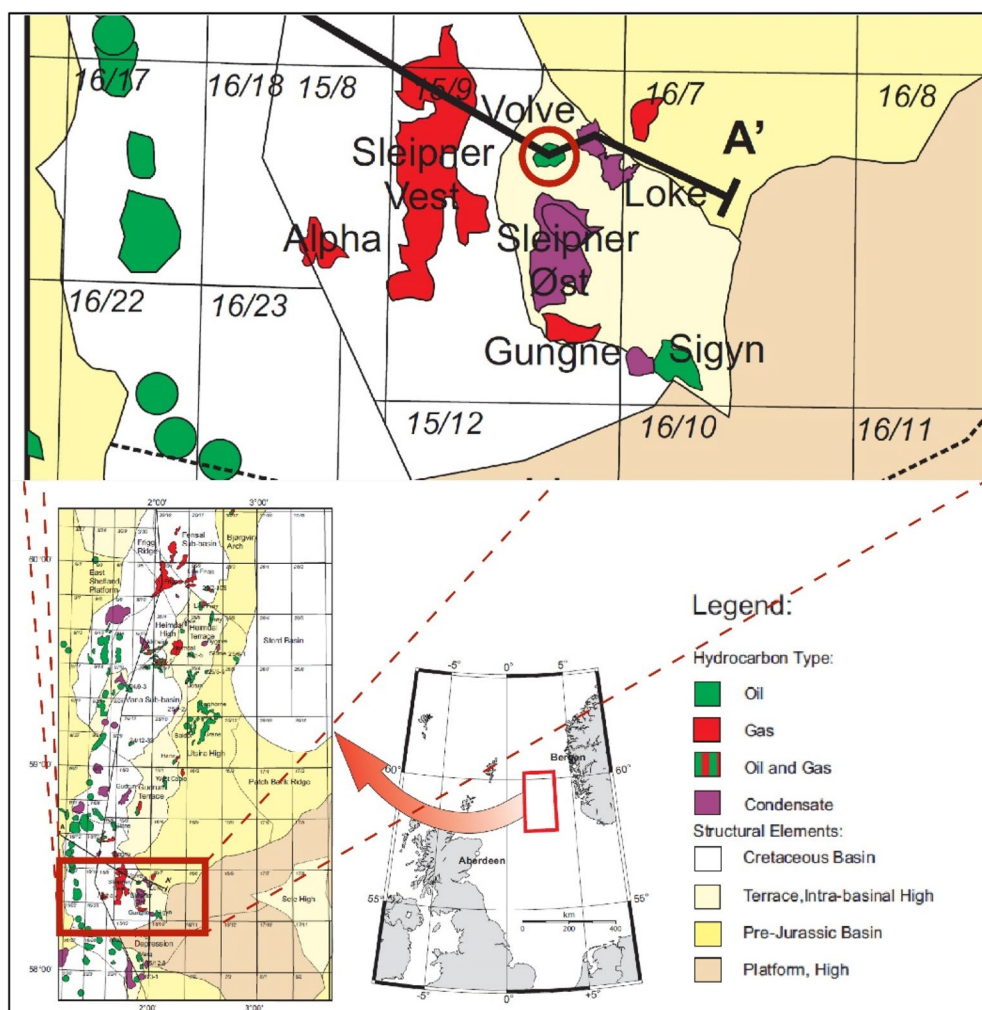


**Fig. 1** Location of Volve field and hydrocarbon producing fields (modified after Justwan 2006)

gas and condensate. Triassic Skagerrak Formation is tight due to dolomite and kaolinite cementation and poor reservoir quality. Jurassic Hugin Formation shows the occurrence of oil with good reservoir quality. Core data and petrophysical log illustrate an average of 22.6% porosity and 914 mD permeability for the Hugin Formation. Also, core sample analysis of Hugin formation at well 15/9-19SR indicates a marine depositional environment. Well log, mud log, lithology description and biostratigraphy analysis help define the age of Hugin formation to be of Callian age. Lithology in Hugin Formation predominantly consists of sandstone. Grains are mainly fine to medium and friable with moderate cementation.

X-Ray Diffraction (XRD) analysis indicates 55–94 weight percentage of quartz and k-feldspar. Clay minerals mainly consist of kaolinite (3–28 weight %) and a minor amount of illite. Drill Stem Test (DST) at 15/9-19SR well suggests that gas has a normal hydrocarbon composition generally found in the North Sea. The isotope value ranges from methane to ethane, propane, and butanes (Statoil, 1993). Due to the complex pattern of isotopes in the gas sample, the actual source of the gas was difficult to identify. However, it was concluded that the gas source

**Fig. 2** Generalised stratigraphic sequence of South Viking graben, North Sea basin from Triassic to Tertiary (Justwan 2006)

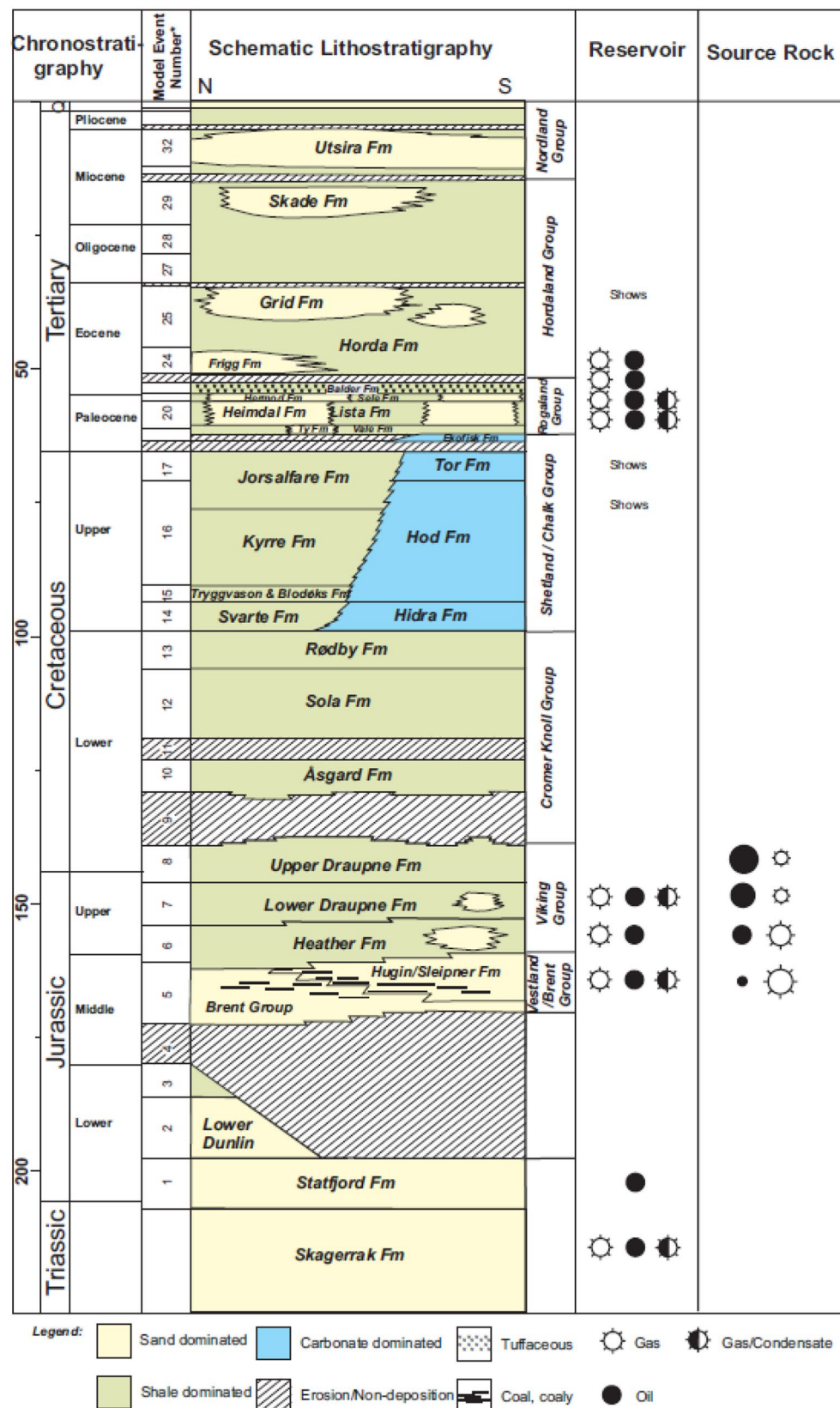


**Table 1** Data inventory in three wells for well based geomechanical model

Well name	Profile	G	R	D	N	CS	SS	A	V	I	C	FP	CT	L	M	DR
15/9-19A	Inclined	Y	Y	Y	Y	Y	Y	No	Y	N	Y	Y	Y	Y	Y	Y
15/9-19B & BT2	Inclined	Y	Y	Y	Y	Y	Y	No	Y	N	Y	Y	Conventional	N	Y	Y
15/9-19S & SR	Inclined	Y	Y	Y	Y	Y	N	No	Y	N	Y	Y	Conventional	Y	Y	Y

G gamma, R resistivity, D density, N neutron, CS compressional slowness, SS shear slowness, A anisotropy, V VSP, I image, C Caliper, FP formation pressure, CT core testing, L LOT, M Mudlog, DR drilling report

could be due to the thermal degradation of inorganic carbonate.

Oil found in Hugin Formation in the Theta vest structure is unique compared to other structures in the Sleipner area, where source rock is expected to be marine. The migration path is different for Theta vest Hugin Formation compared to Sleipner Øst and Loke structure. Though it is not fully clear about the migration path in the Theta Vest area, however, based on structural interpretation and hydrocarbon analysis, a possible migration path can be inferred across the main fault from west and north where the strike of the main fault gradually changes from N–S to NE–SW. It also assumed that oil in the Theta vest Hugin Formation could not be migrated from the Loke, the Sleipner Øst or the Theta vest structure as the Equinor report indicates.

In the Theta vest area, three wells such as 15/9-19S and SR, 15/9-19A, 15/9-19B and BR were selected for the analysis. Among them, 15/9-19S and SR was discovered well and drilled until the Triassic Skagerak formation. Table 1 shows the data inventory chart in these three wells for well based geomechanical modelling. Core-based rock mechanical testing is available in 15/9-19A well in Hugin formation, primarily a hydrocarbon-bearing formation. Thus, proper calibration of rock mechanical property can only be done for Hugin Formation. Formation pressure data were available in all three wells within the primary reservoir sections. However, vertical seismic profile (VSP) and density data were used for overburden sediments, along with drilling events for pore pressure estimation. No image log and multi-arm caliper data were available in three wells. All three wells contain acoustic-compressional and shear slowness and VSP data.

### 3 Geomechanical model parameter

The geomechanical model yields a complete understanding of three principal stresses (one vertical and two horizontal), pore pressure, horizontal stress orientation and rock mechanical properties. Proper scrutiny and quality check of data are essential to establish a well based 1D geomechanical model and minimise uncertainty. In this section, various geomechanical parameters and their calculation methodologies are discussed.

#### 3.1 Vertical stress ( $S_v$ )

In the subsurface, at a given reference point, the vertical stress imposed by the weight of the overlying formation (rocks and water bodies) is called the overburden pressure that holds its importance in determining the fracture pressure of the rock (Zhang 2019). In an offshore, the overburden stress can be expressed as the integration of water density ( $\rho_w$ ) and the formation density ( $\rho_b(Z)$ ) (Zoback et al. 2003).

$$S_v = \rho_w g Z_w + g \int_{z_w}^z \rho_b(Z) dZ \quad (1)$$

where,  $\rho_w$ : density of sea water,  $g$ : acceleration due to gravity,  $Z_w$ : water depth,  $\rho_b(Z)$ : bulk density of the formation as a function of depth, and  $Z$ : depth of the target formation,  $\rho_w$  is the stress component due to the water column, and for onshore wells, this term will be zero. As the present study is offshore, the whole equation is valid for  $S_v$  calculation.

### 3.2 Pore pressure and pore pressure profile ( $P_p$ )

Abnormal formation compaction leads to abnormal pore pressure, particularly overpressure, leading to various non-productive time losses during drilling and can cause accidents such as blowouts and washouts. So, to avoid any drilling mishaps, accurate pore pressure prediction is quite an essential practice before the start of drilling, during, and after drilling (Zhang 2011).

A slow sedimentation rate or normal compaction results in a hydrostatic pore pressure by maintaining an equilibrium between the increasing overburden and decreasing pore-fluid volume. In contrast, rapid sedimentation or rapid compaction leads to faster expulsion of pore-fluids. In such a situation, partial removal of pore-fluids occurs in the less permeable formation. The remaining pore-fluid must support the overburden pressure, which gives rise to an over-pressure region.

The pore pressure profile is estimated based on Terzaghi's effective stress formulation introduced in 1923 (Eq. 2). The effective stress principle says that if hydrocarbon/fluid is extracted from a reservoir, pore pressure will decrease, and effective stress will increase provided no change in overburden stress. Later, Biot generalised Terzaghi's theory described non-linearity between the stress field and pore pressure field and introduced a coefficient as compressibility function (Biot 1941). Biot and Willis (1957) later expressed the relation (Eq. 2) in terms of bulk modulus (Eq. 3).

$$\sigma' = \sigma - \alpha P \quad (2)$$

$$\alpha = 1 - \frac{k_b}{k_g} \quad (3)$$

where,  $\sigma$ : external stress,  $P$ : formation pore pressure,  $\sigma'$ : effective stress,  $\alpha$ : Biot's coefficient,  $k_b$ : formation bulk modulus,  $k_g$ : grain bulk modulus.

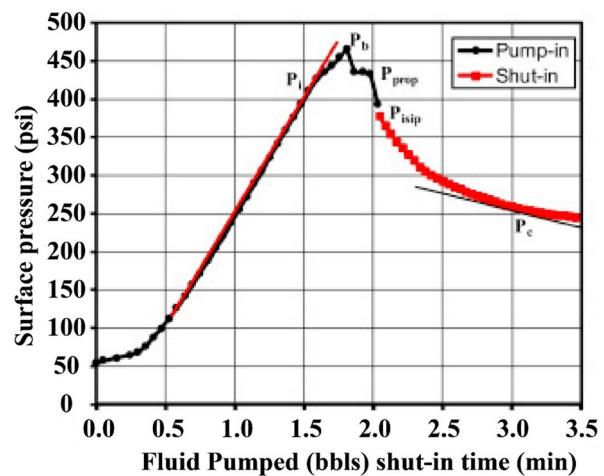
In Terzaghi's relation, it is only one-directional stress, i.e. vertical stress, and in Biot and Willi relation, it is stress tensor, i.e. average of all three principal stresses. Zhang (2011) reported various empirical relations for pore pressure prediction proposed by several researchers. Gardner et al. (1974) and Hottman and Johnson (1965) first proposed empirical relation between formation pressure using P-wave

slowness in Miocene and Oligocene shale in Upper Texas and South Louisiana Gulf Coast (Zhang 2011). Later, Eaton (1972) and Eaton (1975) proposed resistivity based and sonic compression transit time-based relations. Eaton's (1972) resistivity equation is applicable in young sediments, and normal shale resistivity is assumed to be constant. Eaton's sonic relation does not consider the unloading effect (Eaton 1975). However, changing the normal compaction trend line or increasing the exponent under the compaction effect can be captured by the modified Eaton method (Bowers 1995). Bowers (1995) proposed an empirical relation based on compressional transit time under compaction and unloading mechanisms. A recent development in pore pressure prediction from geophysical log data by Traugott (1997) shows sonic velocity derived pore pressure. It is considered that shale porosity decreases exponentially with increasing overburden stress (Athy 1930; Zoback 2007). The normal compaction trend method is used in this study to predict pore pressure in shale layers which is further calibrated with drilling events such as trip gas, static mud weight etc. For sand and carbonate formations, the pore pressure trend is calibrated with formation pressure data and well events such as pump-off gas, trip gas, inflow etc.

### 3.3 Minimum horizontal stress ( $S_{hmin}$ ) magnitude

Minimum horizontal stress ( $S_{hmin}$ ) and fracture pressure gradient (FG) were calculated and calibrated based on a leak-off test (LOT), extended leak-off test (XLOT), microfrac and minifrac data and drilling events such as loss circulation or ballooning etc. The formation integrity test (FIT) is not considered for minimum stress calibration as it is lower than the fracture initiation pressure.  $S_{hmin}$  or FG is essential for drilling operations to prevent the mud loss and get a safe mud window. In a typical XLOT (Fig. 3) test, fluid is pumped at a constant flow rate below the casing shoe (Zhang 2019). Pressure vs volume or pressure vs time plot shows a linear trend until it reaches fracture initiation pressure ( $P_f$ ), identified as deflection in a linear trend. If pressure increases, formation breakdown pressure is achieved, identified as a sudden pressure drop in the curve. This point is called formation breakdown pressure ( $P_b$ ). After this point, pressure remains almost the same with a constant flow rate. The pressure curve appears as a horizontal

**Fig. 3** Typical XLOT curved presented as surface pressure vs volume or time (Zhang 2019)



line in the plot, indicating propagation of an already created fracture. This pressure is called fracture propagation pressure ( $P_p$ ). After turning off the pump, the pressure suddenly dropped to instantaneous shut-in pressure ( $P_{isip}$ ). When the shut-in pressure gradually drops to fracture closure pressure ( $P_c$ ), Shmin is considered fracture closure pressure. On the other hand, the fracture pressure gradient is fracture initiation pressure. Thus, the  $S_{hmin}$  value is more conservative than the fracture gradient to define the upper bound of mud weight.

Several approaches have been developed to get continuous minimum horizontal stress, which needs further correlation with the above-mentioned direct measurement data set. This study adopts the effective stress ratio (ESR) method to achieve the minimum horizontal stress profile (Eq. 4). Due to its minimum input parameters, minimum horizontal stress, vertical stress, and pore pressure, it is easy to implement the ESR method compared to the log derived stressed model. Log derive stress methodology requires Poisson's ratio, Young's modulus and tectonic strain factors, making it challenging to calibrate (Fang and Khaksar 2012; Zoback 2007). The effective stress ratio,  $k_o$ , is expressed as mentioned below:

$$k_o = \frac{S_{hmin} - P_p}{S_v - P_p} \quad (4)$$

### 3.4 Rock mechanical properties

Rock mechanical properties include uniaxial compressive strength (UCS), Young modulus (E), Poisson's ratio ( $\nu$ ), internal friction coefficient (IF), cohesion ( $S_o$ ). Rock mechanical properties can be achieved by direct measurements, laboratory-based rock mechanical testing using cores and the indirect method using petrophysical log data (Khaksar et al. 2009). Mechanical properties measured using rock cores provide point information, whereas log derived results give continuous values. However, it is always necessary to calibrate log derived rock mechanical properties with the core data to reduce uncertainty in the model.

Indirect estimation of mechanical properties (elastic modulus and Poisson's ratio) of rocks is often done by using the ultrasonic wave velocities of the rock, such as longitudinal and transverse wave velocity. Rock properties measured using such ultrasonic wave velocities are termed dynamic rock properties. Poisson's ratio ( $\nu$ ) can be estimated by using Eq. 5.

$$\nu = \frac{V_p^2 - 2V_s^2}{2(V_p^2 - V_s^2)} \quad (5)$$

Dynamic Young's modulus ( $E_{dyn}$ ) can be estimated using Eq. 6.

$$E_{dyn} = \rho V_s^2 \left( \frac{3V_p^2 - 4V_s^2}{V_p^2 - V_s^2} \right) \quad (6)$$

where,  $V_p$ : compressional wave velocity,  $V_s$ : shear wave velocity,  $\rho$ : density of the rock.

### 3.5 Maximum horizontal stress ( $S_{Hmax}$ ) orientation

Horizontal stress orientation is one of the significant parameters of a geomechanical model as wellbore failure, and optimum mud weight is governed by stress azimuth. A common approach in identifying stress orientation is the analysis of logging while drilling (LWD), wireline image log data for breakouts and tensile fractures, and multi-arm (4 arm/6 arm) caliper data. Due to stress concentration around the wellbore, we may observe breakouts if there is a significant difference between  $S_{Hmax}$  and  $S_{hmin}$ . In the Kirsch model, a formation is assumed to be isotropic and elastic, and three principal stresses are perpendicular to each other, with the wellbore axis parallel to vertical stress (Zoback 2007). Horizontal stresses are concentrated around the wellbore and create hoop stress. Maximum hoop stress is concentrated towards far-field minimum stress and creates a compressional zone at the near-wellbore. When the stress concentration is higher than rock strength, breakouts appear in the wellbore at  $180^\circ$  apart. On the other hand, towards the direction of the  $S_{Hmax}$ , a tensile zone is created, and tensile fractures tend to develop if tensile stress exceeds rock tensile strength. Thus, breakouts and drilling induced tensile fracture's azimuth in vertical wellbore help get stress orientation.

Figure 4 schematically illustrates the position of breakouts and tensile fractures along the well periphery for  $S_{Hmax}$  azimuth. In the absence of an image log or multi-arm caliper data, earthquake focal mechanism and lithospheric flexure method can be implemented (Grollimund and Zoback 2003). World stress map is a reference database that provides a good understanding of horizontal stress azimuth throughout the globe (Heidbach et al. 2018, 2010; Zoback and Zoback 1989).

### 3.6 Maximum horizontal stress ( $S_{Hmax}$ ) magnitude constrain

Determining the  $S_{Hmax}$  magnitude is the most critical and challenging task in every geomechanical modelling workflow as there is no direct measurement approach to calibrate  $S_{Hmax}$  magnitude as compared to  $S_{hmin}$  magnitude. To constrain the  $S_{Hmax}$  magnitude

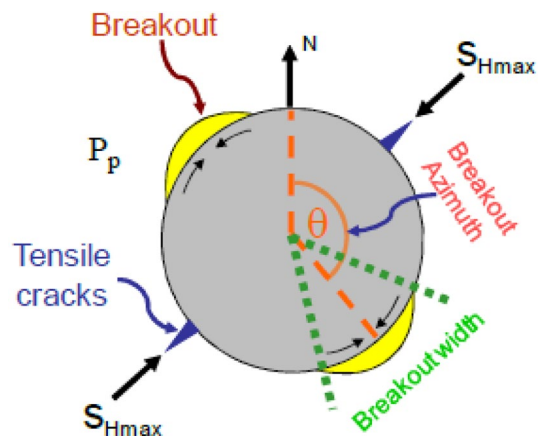


**Fig. 4** Schematic representation of circular wellbore,  $S_{Hmax}$  azimuth, breakouts and tensile fracture azimuth

stress polygon method has been adapted based on frictional fault theory (Zoback 2007). The theory suggests that at a given depth for known pore pressure and overburden stress, the stress in the earth's crust is restricted by fault frictional strength of the fault. Based on Anderson's classification, stress regimes are normal, strike-slip, and reverse based on the relative magnitude of three principal stresses that the Coulomb failure criterion can predict (Eq. 7). Based on breakout width, rock strength and pore pressure,  $S_{Hmax}$  can be calculated based on Eq. 8 (Barton et al. 1988; Barton 1987; Zoback 2007). Equation 8 and stress polygon combined can facilitate to constrain  $S_{Hmax}$  magnitude and stress regime. They are listed as follows:

$$\frac{\sigma_1 - P_p}{\sigma_3 - P_p} = \left( \sqrt{\mu^2 + 1} + \mu \right)^2 \quad (7)$$

$$S_{Hmax} = \frac{(C_o + 2P_p + \Delta P + \sigma^{\Delta T}) - S_{hmin}(1 + 2 \cos 2\theta_b)}{1 - 2 \cos 2\theta_b} \quad (8)$$

where,  $\mu$ : fault frictional coefficient,  $2\theta_b \equiv \pi - W_{bo}$  (Breakout width),  $C_o$ : uniaxial compressive strength (UCS).

### 3.7 Collapse pressure estimation and wellbore stability analysis

Understanding collapse pressure is essential for wellbore stability analysis as it governs the lower bound

of mud weight, where the collapse pressure gradient exceeds the pore pressure curve. Several engineers and scientists proposed many empirical relations in the past to predict the collapse pressure of the formation. However, a few widely used failure criteria are Mohr–Coulomb, Hoek–Brown failure criterion (Hoek and Brown 1980), Modified Lade (Lade 1977). Each failure criterion has certain limitations; however, they work well in certain conditions. Mohr–Coulomb failure criterion is written as Eq. 9 (Fang and Khaksar 2012).  $\tau$  and  $\sigma_n$  are derived from principal stresses and it is assumed that intermediate stress has no influence (Zoback 2007). Linear failure envelop is the result due to critical combination of  $\sigma$  and  $\tau$  (Labuz and Zang 2012). In Mohr–Coulomb equation two parameters define material property,  $S_0$  and  $\theta$ . Due to its mathematical simplicity, the Mohr–Coulomb failure criterion is widely accepted (Labuz and Zang 2012). As a base case scenario Mohr–Coulomb criterion is run to understand the collapse pressure.

$$\tau = S_0 + (\sigma_n - P_p) \tan \theta \quad (9)$$

where,  $\tau$ : shear stress component acting parallel to the shear plane,  $S_0$ : cohesion,  $\sigma_n$ : normal stress component acting on the shear plane,  $P_p$ : pore pressure,  $\theta$ : angle of internal friction.

The second failure criterion is the Hoek–Brown failure criterion tested in this work. This failure criterion is evolved based on several laboratory triaxial test data for the brittle failure of intact rock mass (Eberhardt 2012). The following equation defines the non-linear Hoek–Brown failure criterion for intact rock (Eberhardt 2012; Hoek and Brown 1980).

$$\sigma_1 = \sigma_3 + \sqrt{mC_0\sigma_3 + sC_0^2} \quad (10)$$

where,  $\sigma_1$ : major principal stress at failure,  $\sigma_3$ : minor principal stress at failure,  $C_0$ : uniaxial compressive strength of intact rock,  $m$  &  $s$ : dimensionless empirical constants.

Similar to the Mohr–Coulomb criterion, there is no influence of intermediate stress in the Hoek–Brown criterion. Parameter  $m$  and  $s$  in the Hoek–Brown equation are analogous with the Mohr–Coulomb equation's frictional strength and rock mass cohesion. While the large value of  $m$  represents strong brittle rock, which corresponds to high instantaneous frictional angles, the lower value represents ductile rocks

having low instantaneous frictional angles. Parameter  $s$  defines fracture intensity, and value ranges from 1 for intact rock to 0 for heavily fractured rock. The range of parameter  $m$  varies for different rock types. While for sandstone and quartzite, this value ranges from 15 to 24; in mudstone, silt, shale slate, it ranges from 4 to 10 (Zoback 2007), upon comparison non-linear Hoek–Brown criterion represents an accurate value of intact rock strength than the linear Mohr–Coulomb criterion (Eberhardt 2012; Ghazvinian et al. 2008; Zhao 2000). Pariseau (2007) also showed that the non-linear Hoek–Brown criterion represents better fitting than Mohr–Coulomb and Drucker–Prager criterion. No influence of intermediate principal stress on all these criteria is assumed in this analysis. Several researchers also highlighted that as intermediate stress significantly influences rock strength, Eq. 10 may not accurately represent the rock failure criterion. However, the Hoek–Brown criterion established using extensive laboratory measurements covers a broad spectrum of intact rock types, and non-linear failure envelops fitting well in laboratory rock testing data.

Though the above-mentioned two failure criteria are easy to imply and most of the cases lead to valuable results, the influence of intermediate principal stress on rock failure is ignored. Studies indicate a substantial contribution of intermediate principal stress on rock strength (Eberhardt 2012). Modified Lade failure criterion is one of the failure criteria where intermediate principal stress is considered. The equation was introduced by Ewy (1999) from the original formula (Lade 1977) as mentioned in Eqs. 11–15 (Zoback 2007)

$$\frac{(I'_1)^3}{I'_3} = 27 + \eta \quad (12)$$

where,

$$I'_1 = (\sigma_1 + S) + (\sigma_2 + S) + (\sigma_3 + S) \quad (13)$$

$$I'_3 = (\sigma_1 + S)(\sigma_2 + S)(\sigma_3 + S) \quad (14)$$

$S$  and  $\eta$  are material constant and can be defined as below, where  $S_0$  is cohesion and  $\theta$  is the internal frictional angle.

$$S = \frac{S_0}{\tan \theta} \quad (15)$$

$$\eta = \frac{4 \tan^2 \theta (9 - 7 \sin \theta)}{1 - \sin \theta} \quad (16)$$

Modified Lade criterion shows how rock strength initially increases with increasing value of  $\sigma_2$  followed by a reduction of strength. Ewy (1999) shows the application of the Modified Lade failure criterion in wellbore stability. The result indicates that the Mohr–Coulomb criterion predicts higher mud weight for the same trajectory of a wellbore than the Modified Lade failure criterion. He also highlighted that the Druker–Pager criterion predicts the least mud weight. All the mentioned failure criteria were applied to understand the best possible failure mechanism in this analysis.

## 4 Result and discussion

### 4.1 Vertical stress ( $S_v$ ) gradient

Density data for all wells in the reservoir section are available. VSP based pseudo-density curve is used where density log data is not obtained. At the mud line, density is 1.66 gm/cc (Tenzer and Gladkikh 2014). Density logs have been recorded from Lista Formation to Hugin Formation. Interval velocity from VSP data from Skade Formation (~1190 m true vertical depth rotary table (TVDRT)) to Tor Formation, and acoustic derived density data is considered shallow formation. However, the missing density log from the mud line to the shallowest recorded point is compensated by an exponential curve. Table 2 shows the average density values for each formation ranging from Skade to Hugin formation. The equation of the exponential curve is defined by Eq. 17. Figure 5 shows the overburden stress profile in absolute (psi) and equivalent mud weight (ppg) term along the well profile for 15/9-19SR well. The vertical stress gradients appear at the reservoir section around ~17 ppg.

$$y = c + ae^{xb} \quad (17)$$

where,  $a$  ( $\text{kg}/\text{m}^3$ ) = -912.889,  $b$  ( $1/\text{m}$ ) = -0.000676,  $c$  ( $\text{kg}/\text{m}^3$ ) = 2516.944

**Table 2** Average density recorded from Skade to Hugin Formation

Formation	Average density (g/cc)
Skade	2.25
Grid	2.28
Balder	2.40
Sele	2.49
Lista	2.41
Heimdal	2.18
Tor	2.57
Hod	2.56
Blodoks	2.63
Hidra	2.65
Rodby	2.66
Sola	2.64
Asgard	2.62
Draupen	2.30
Heather	2.60
Hugin	2.27

### 4.2 Pore pressure ( $P_p$ )

Based on acoustic and VSP data, Eaton based normal compaction method is implemented for shale layers. Further calibration with mud weight and drilling events such as connection gas, background gas is done to estimate the pressure profile from the mud line. Slope of Normal compaction for shallow shale layers around ~7855 and Eaton exponent is considered as 3. Direct pressure measurements and drilling responses estimate the pressure profile for carbonate and sand layers. Table 3 shows the measured pressure gradient in the ppg unit recorded from different formations.

Figure 5 shows pore pressure (blue curve) and overburden stress (black curve) profile at 15/9-19SR well location. The pressure profile appears to be hydrostatic till Hordaland and gradually increases from above the top of Skade Formation to around 11.10 ppg. At the bottom of the Skade Formation, pressure reversal is observed until the Grid Formation is calibrated with the trip gas event. Pressure profile in Skade Formation is calibrated interpreted with trip gas and mud weight.

From the Grid Formation to the top of the Shetland Group, pressure appears to be hydrostatic or slightly above hydrostatic. Pressure points acquired in Grid,

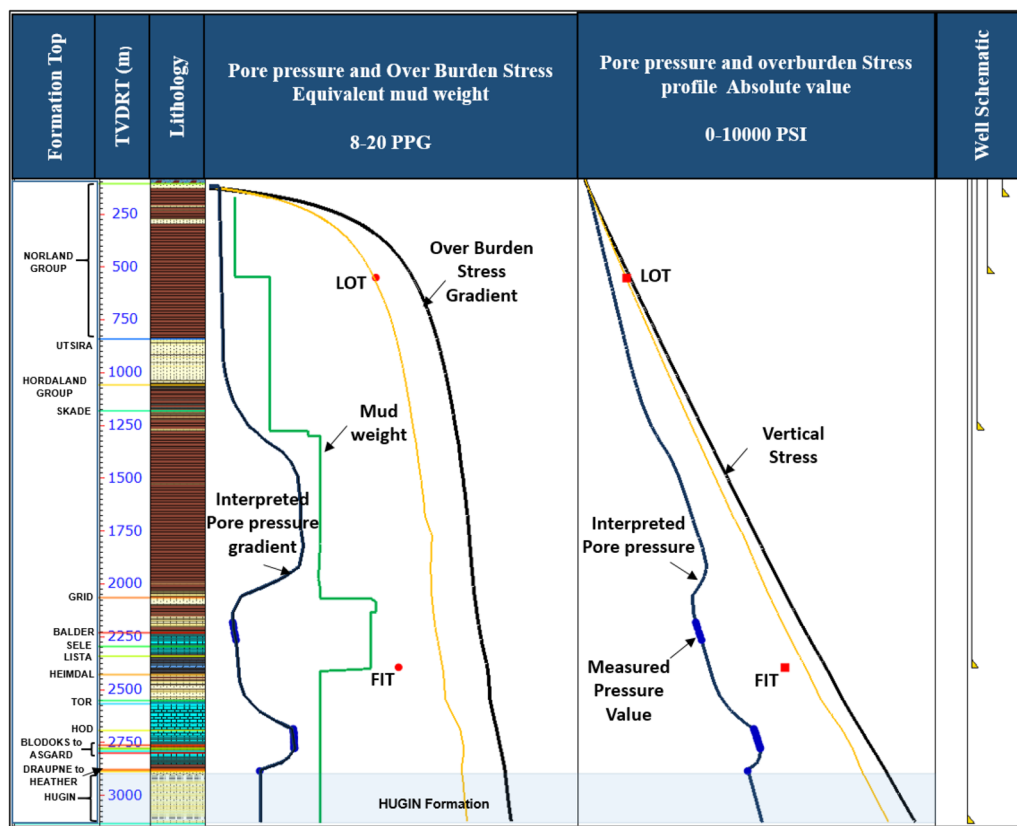


**Fig. 5** Pore pressure (Blue curve), Overburden stress (Black Curve), Fracture gradient (Yellow curve) along with mud weight (green curve) and LOT/FIT (red square) at well location 15/9-19SR

and Balder Formations (blue dots) shows around 8.86 ppg pressure gradient.

Another pressure ramp was observed from the Shetland Group until the bottom of Tor Formation up to 10.79 ppg, calibrated with pressure points taken in Tor, Hod, Blodoks and Hidra Formation. Further pressure reversal was observed, and in Hugin Formation, the pressure gradient appears to be 9.61 ppg, which continues till total depth (TD).

#### 4.3 $S_{h\min}$ magnitude

Only one LOT value is available in the target well in 13-3/8" casing shoes. In well 15/9-19S & SR at 9-5/8" casing shoe (2395.25 m TVDRT), FIT (Formation integrity test) is taken inside Lista Formation. However, 15/9-19A well shows two LOT values at 9-5/8" casing shoe (1639.62 m and 1655.80 m TVDRT), which is inside Skade Formation. Table 4 summarises recorded LOT and FIT values in the ppg unit. Due

to a limited LOT data set, several pieces of literature and published data set were taken as a reference to get the value of  $k_o$  for the North Sea region. Figure 6 shows the values of  $k_o$  around the world based on LOT data. In the plot for the North Sea area (blue triangle),  $k_o$  value ranges from 0.6 to 1. The most likely value is the cyan colour line (Zhang and Yin 2017). For the present study,  $k_o$  is estimated at around 0.83 based on LOT values. As no closer pressure curve value is provided, these LOTs are considered near or above fracture initiation pressure ( $P_i$ ), which is less conservative. Thus, the given LOT values are precisely considered a fracture gradient over the  $S_{h\min}$  value. Figure 5 shows fracture gradient curved (yellow curve), LOT and FIT values, pore pressure, and overburden gradient and stress. The fracture gradient in Hugin Formation appears around 15.56 ppg. It is also noticed that the estimated fracture gradient at the same TVD (~1639.62 m to 1655.80 m) in Skade

**Table 3** Direct pressure measurement values in equivalent mud weight (EMW) (ppg) unit at 15/9-19SR well

Formation	TVDRT (m)	Measure pressure EMW (ppg)
Grid	2182.63	8.77
	2193.34	8.79
	2208.91	8.81
Balder	2231.42	8.83
	2247.04	8.86
	2266.51	8.88
Tor	2686.38	10.77
	2690.38	10.77
Hod	2698.2	10.77
	2701.69	10.78
	2705.58	10.79
	2711.04	10.79
	2722.67	10.79
	2726.88	10.79
	2730.08	10.79
	2732.81	10.79
	2739.26	10.79
Blodoks	2745.89	10.79
	2752	10.79
	2764.69	10.81
Hidra	2770.36	10.79
	2777.56	10.82
	2779.64	10.79
Hugin	2885.9	9.66

Formation is around ~ 15 ppg (~29 MPa), which is a little higher than measure LOT values.

#### 4.4 Rock mechanical properties

Rock mechanical testing data is available in well 15/9-19A from Hugin Formation. Table 5 shows the core inventory for rock mechanical testing. Eight-core plugs have been extracted from these two core samples, and rock mechanical testings have been carried out. Figure 7 shows the core image before and after the single-stage destructive test (Khaksar et al. 2009)

of four core plugs (1G, 2G, 3G and 4G) from 3870.50 to 3870.70 m depth. Figure 7 also describes the failures of values during testing. It is visible that core plugs underwent failure along the shear plane after each destructive test. Data are plotted in Mohr space (Shear stress vs Normal Stress) and  $\sigma_1 - \sigma_3$  space to establish UCS, IF and cohesion ( $S_o$ ) value (Figure 8). Similar analysis is carried out for the core plug samples from 3887.30 to 3887.50 m. Table 6 depicts the rock mechanical properties of the Hugin Formation based on core testing.

Continuous rock mechanical properties were calculated from the acoustic log, density log and calibrated with core measured data. Figure 9 indicates calibrated rock mechanical properties of the Hugin Formation.

Dynamic Poisson's ratio shows a significant match with core data. However, dynamic Young's modulus needs further calibration to match with core tested data and get the static Young's modulus. A statistical analysis has been done to get the  $P_{10}$ ,  $P_{50}$  and  $P_{90}$  values of UCS (Fig. 9b). The statistical distribution shows UCS range is around 33–39 MPa (Table 7).

#### 4.5 Maximum horizontal stress ( $S_{Hmax}$ ) orientation

Due to the absence of multi-arm caliper and available image log, reference from world stress map (Zoback and Zoback 1989) and previously done regional study were considered. Grollimund and Zoback (2003) and (Zoback 2007) showed maximum stress orientation near Viking graben as approximately E–W. However, stress rotation is prominent from NW–SE to NE–SW across the Viking graben from West to East (Figure 10). Wiprut (2001) shows the stress orientation approximately E–W of the Visund field (Fig. 10a). The above reference study has been considered to understand the stress orientation, approximately E–W in the present studied field, and marked in the red circle in Fig. 10.

**Table 4** Acquired LOT and FIT values in 15/9-19SR&S and 15/9-19A well in ppg unit

Well	Casing	Depth TVDRT (m)	LOT EMW	Type of test
15/9-19S & SR	13 3/8	551.99	13.49	LOT
15/9-19S & SR	9 5/8	2395.25	14.24	FIT
15/9-19A	9 5/8	1639.62	14.44	LOT
15/9-19A		1655.80	14.41	LOT

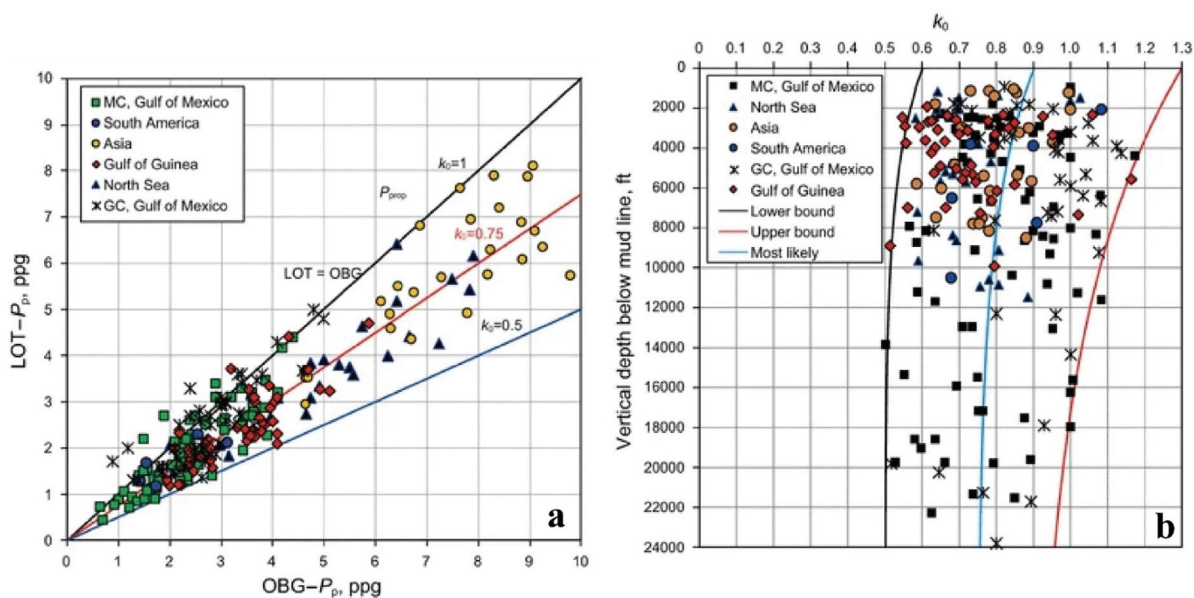


**Fig. 6** Plot (a) shows the distribution of  $k_o$  value derived from LOT data acquired in different basins worldwide (Gulf of Mexico, South America, Asia, North Sea). Plot (b) depicts a

similar  $k_o$  value with depth (TVDSS). North Sea data are represented by a blue triangle and lie between 0.6 to 1 (Zhang and Yin 2017)

**Table 5** Core inventory for rock mechanical testing

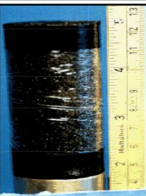
Well no	Depth of seal peel MD (RKB) m	Test no	File no	Depth of test	Initial specimen height (mm)	Initial specimen diameter (mm)	Lithology
15/9-19A	3870.50–3870.70	1G	TRI 438	3870.52	88.84	37.81	Sandstone
		2G	TRI 440	3870.57	80.54	37.67	
		3G	TRI 441	3870.61	81.58	37.8	
		4G	TRI 444	3870.66	81.01	37.81	
	3887.30–3887.50	5G	TRI 445	3887.32	83.55	37.87	
		6G	TRI 446	3887.37	81.9	37.87	
		7G	TRI 448	3887.41	83.14	37.37	
		8G	TRI 451	3887.46	82.11	37.85	

#### 4.6 $S_{H\max}$ magnitude constrain

Based on stress polygon theory discussed in Sect. 3.6,  $S_{H\max}$  magnitude has been estimated at reservoir interval in well 15/9-19A. Pore pressure and fracture gradients are the same as well 15/9-19SR since reservoir targets are not too far. As no breakouts were observed in the available image log, two scenarios were run considering  $0^\circ$  and  $45^\circ$  breakout width. The inclination of the well at the reservoir section is around  $26^\circ$  and azimuth  $33^\circ$ .  $P_{10}$  value, 4863 psi

(34 MPa) calibrated UCS is considered for a lower bound of estimation of  $S_{H\max}$ .

Internal friction 0.6,  $S_{h\min}$  gradient 15.76 ppg, (~72 MPa)  $S_v$  17 ppg (~77 MPa) and pore pressure 9.61 ppg (~44 MPa) were considered for the analysis at 3868.82 m (12693ft) TVDRT. Scenario-I (breakout width  $0^\circ$ ) (Fig. 11a) shows  $S_{H\max}$  magnitude constrains between 20.27 ppg (~92 MPa) from weak rock and 22 ppg (~100 MPa) for strong rock. Scenario-II (breakout width  $45^\circ$ ) (Fig. 11b) depicts  $S_{H\max}$  range around 21–23 ppg (~95–105 MPa). Baker Hughes,

Test No	Before Test	After Test	Failure Values
1G			Vertical effective stress (MPa): 32.07 Horizontal effective stress (MPa): 2.01 Shear stress (MPa): 15.03 Vertical strain (mS): 3.59 Horizontal strain (mS): -3.66
2G			Vertical effective stress (MPa): 69.63 Horizontal effective stress (MPa): 7.51 Shear stress (MPa): 31.06 Vertical strain (mS): 5.39 Horizontal strain (mS): -4.26
3G			Vertical effective stress (MPa): 96.28 Horizontal effective stress (MPa): 14.98 Shear stress (MPa): 40.65 Vertical strain (mS): 7.04 Horizontal strain (mS): -3.07
4G			Vertical effective stress (MPa): 1225.02 Horizontal effective stress (MPa): 28.63 Shear stress (MPa): 48.19 Vertical strain (mS): 6.06 Horizontal strain (mS): -1.69

**Fig. 7** Core plug (1G, 2G, 3G and 4G) images before and after single-stage destructive testing along with testing parameters. After the test, each core plug shows a distinct plan of shear failure

GMI. SFIB™ software platform used for the analysis and presentation. In the plot, red contour lines represent different UCS values, and blue contours indicate tensile strength. The relative magnitude of three principal stresses indicates a strong strike-slip fault regime ( $S_{\text{Hmax}} > S_v > S_{\text{hmin}}$ ), corroborated with stress polygon analysis.

#### 4.7 Model calibration

Rock mechanical properties such as uniaxial compressive strength, Young's modulus, Poisson's ratio, internal friction, principal stresses, and pore pressure were used as input parameters and calibration to

predict collapse pressure gradient and calibration of the model with the caliper record.

While all the inputs for Mohr–Coulomb and Modified-Lade came from geomechanical parameters, parameters  $m$  and  $s$  in the Hoek–Brown model are 15 and 1, respectively, as the Hugin Formation is characterised as intact sandstone facies. Figure 12 shows the calibration result based on these scenarios. The 2<sup>nd</sup> track indicates predicted and allowable breakout widths in each plot, and the 3<sup>rd</sup> track show caliper and bit size. Except for the top 20 m, no major caliper enlargement is observed in the formation. It is observed that while Hoek–Brown prediction shows a reasonable match with caliper enlargement,

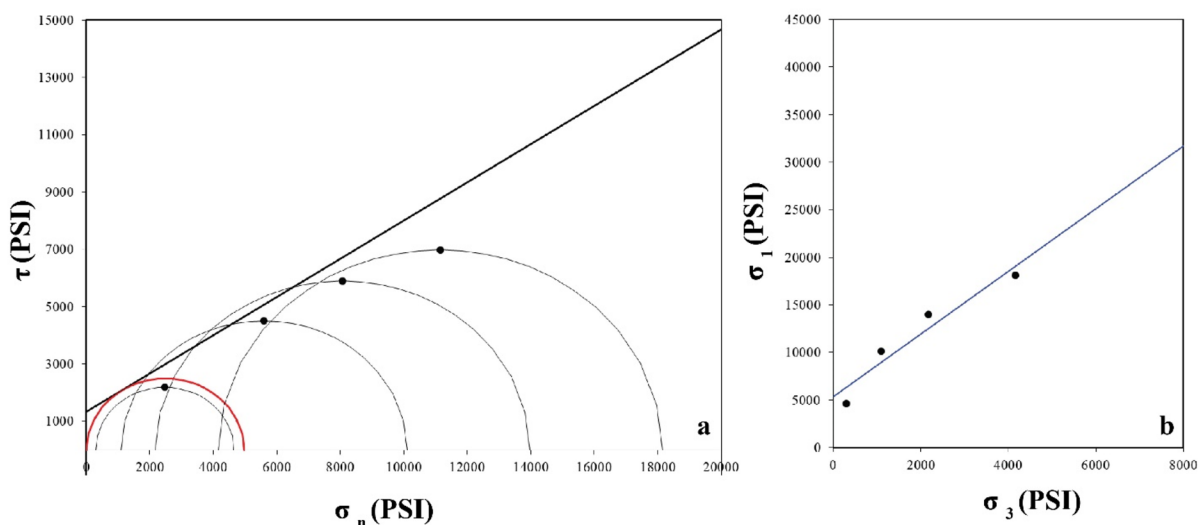


**Fig. 8** Plotting of rock testing data (core plug 1G, 2G, 3G and 4G) in Mohr space (a) and  $\sigma_1 - \sigma_3$  (b) space to ascertain the UCS, IF, and  $S_o$

Mohr–Coulomb criterion shows over prediction, and Modified Lade shows under prediction.

#### 4.8 Azimuthal and inclination sensitivity analysis for mud weight program

After getting fully calibrated models, geomechanical parametric analysis was carried out to understand the optimum mud weight program for future wells. Figure 13a shows lower hemisphere stereonet projection with minimum mud weight in colour code for wellbore stability for all possible well trajectories in Hugin Formation.

Blue colour indicates lower mud weight, and red colour shows the higher end of the mud weight range. Radial lines indicate azimuth and concentric circles represent inclination of  $0^\circ$ ,  $30^\circ$ ,  $60^\circ$  and  $90^\circ$  from the centre to the periphery. The white dot represents studied well inclination and azimuth. From the plot, it can be clearly understood that minimum mud weight requires around 11 ppg for Hugin Formation, having a trajectory of  $36^\circ$  deg azimuth and  $30^\circ$  inclination.

However, the used mud weight is more than 12 ppg for the stability of overlaying shale formations. A similar kind of stereoplot analysis is carried out where colour code represents the optimal mud weight window with azimuthal and inclination sensitivity (Fig. 13b). Both plots suggest that the most appropriate well direction for any high angle well will be towards the  $S_{h\min}$  direction in terms of minimum mud weight (Fig. 13a) and maximum mud weight operation window (Fig. 13b). Wiprut and Zoback (2000) depict stress tensor, rock mechanical properties and wellbore stability analysis in Visund field near the western edge of Viking graben. Their research indicates that a strike-slip fault regime is dominated with  $S_{h\max}$  orientation as approximately E-W. Wellbore stability analysis and stereonet plot of differential pressure indicate that inclined wellbores towards geographic north require higher differential pressure than the E-W direction with  $S_{h\max}$  orientation.

**Table 6** Core testing result and rock mechanical properties in Hugin formation

Well No	Depth of seal peel MD (RKB) m	Test No	File No	Depth of test	CS (MPa)	$\nu$	Values at failure			
					$\varepsilon_v$ (mS)	$\varepsilon_h$ (mS)	Volumetric Strain (mS)	Coefficient of Internal Friction	UCS (MPa)	Cohesion (MPa)
15/9-19A 3870.50–3870.70	1G	TRI 438	3870.52	2	0.46	3.59	-3.66	-3.73	33.68	0.66
	2G	TRI 440	3870.57	7.5	0.31	5.39	-4.26	-3.12		
	3G	TRI 441	3870.61	15	0.26	7.04	-3.07	0.9		
3887.30–3887.50	4G	TRI 444	3870.66	28.7	0.2	6.06	-1.69	2.69		
	5G	TRI 445	3887.32	2	0.42	5.04	-4.99	-4.93		
	6G	TRI 446	3887.37	7.5	0.37	6.55	-4.87	-3.2		
7G	TRI 448	3887.41	15	0.32	8.95	-6.1	-3.25			
	8G	TRI 451	3887.46	28.7	0.25	11.06	-4.46	2.14		

CS: Consolidation stress,  $\nu$ : Poisson's ratio,  $\varepsilon_v$ : Vertical strain,  $\varepsilon_h$ : Horizontal strain,  $\theta$ : Frictional angle

## 5 Conclusion

The present study is focused on the Hugin Formation of the Theta vest structure in the North Sea, one of the oil-producing reservoirs in the Volvo field. The main objectives were to establish a 1D geomechanical model, to understand in-situ stress states and to analyse wellbore stability complications of Hugin Formation based on the available database in the public domain, focusing mainly on three wells where most data sets are available.

- Pore pressure data calibrated with direct pressure measurement, and the gradient shows higher than hydrostatic pressure, ~9.61 ppg.
- The stress state indicates a strong strike-slip fault regime ( $S_{H\max} > S_v > S_{h\min}$ ) within the Hugin Formation. Maximum horizontal stress azimuth is considered to be approximately E-W direction.
- Rock mechanical properties calibrated with available core test data and UCS value ranging from 31 to 41 MPa.
- Model calibration and azimuthal sensitivity analysis suggest that for deviated wellbores in Hugin Formation,  $S_{h\min}$  azimuth, i.e., approximately N–S is the most relevant term of wellbore stability and mud weight window.
- Uncertainties in the model cannot be overlooked due to some data gaps. For  $S_{h\min}$  calibration, no LOT/XLOT curve was available; thus, the value is considered less conservative. For stress orientation, regional data set is considered due to the absence of image log and multi-arm caliper data.  $S_{H\max}$  values also show a wide range.
- Despite uncertainties, the model provides a reasonable understanding of the geomechanical characteristics of the reservoir section and can be considered a base model for further investigation of geomechanical behaviour due to production. Analysis such as fault reactivation due to CO<sub>2</sub> injection and stress behaviour due to production and depletion may be considered for future research.

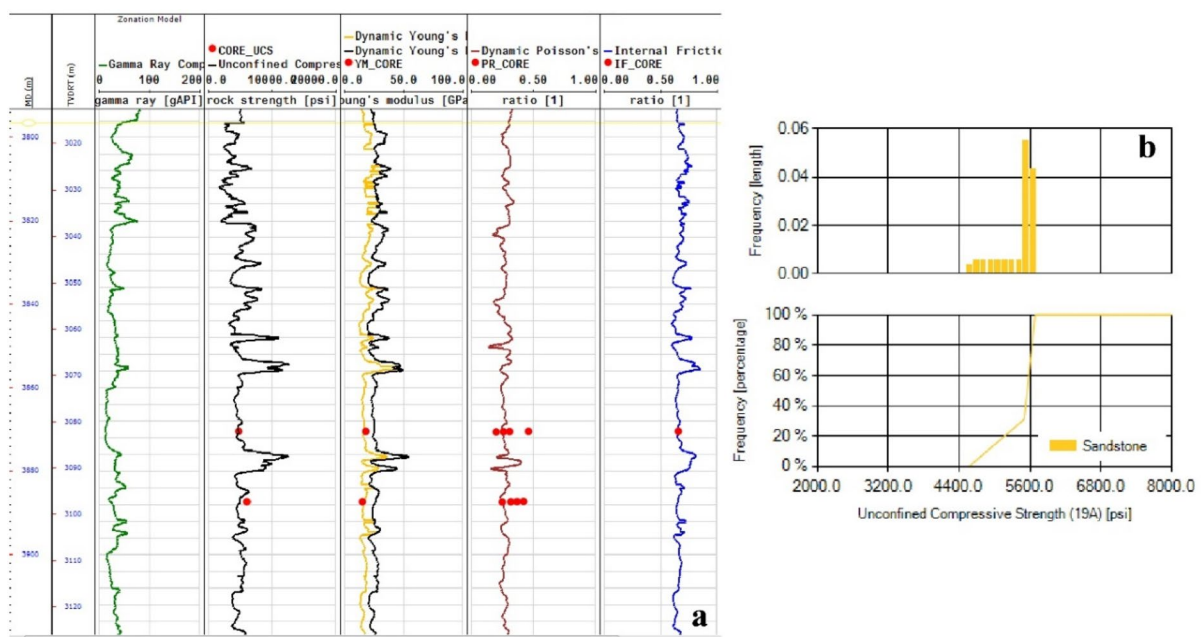


**Fig. 9** (a) Log derived rock mechanical properties calibrated with core resting data in Hugin formation. (b) The statistical distribution of UCS to get  $P_{10}$ ,  $P_{50}$  and  $P_{90}$  values

**Table 7** UCS value distribution Hugin formation

Lithology	UCS		
	$P_{10}$	$P_{50}$	$P_{90}$
Sandstone	4863 psi (~34 MPa)	5546 psi (~38 MPa)	5657 psi (~39 MPa)

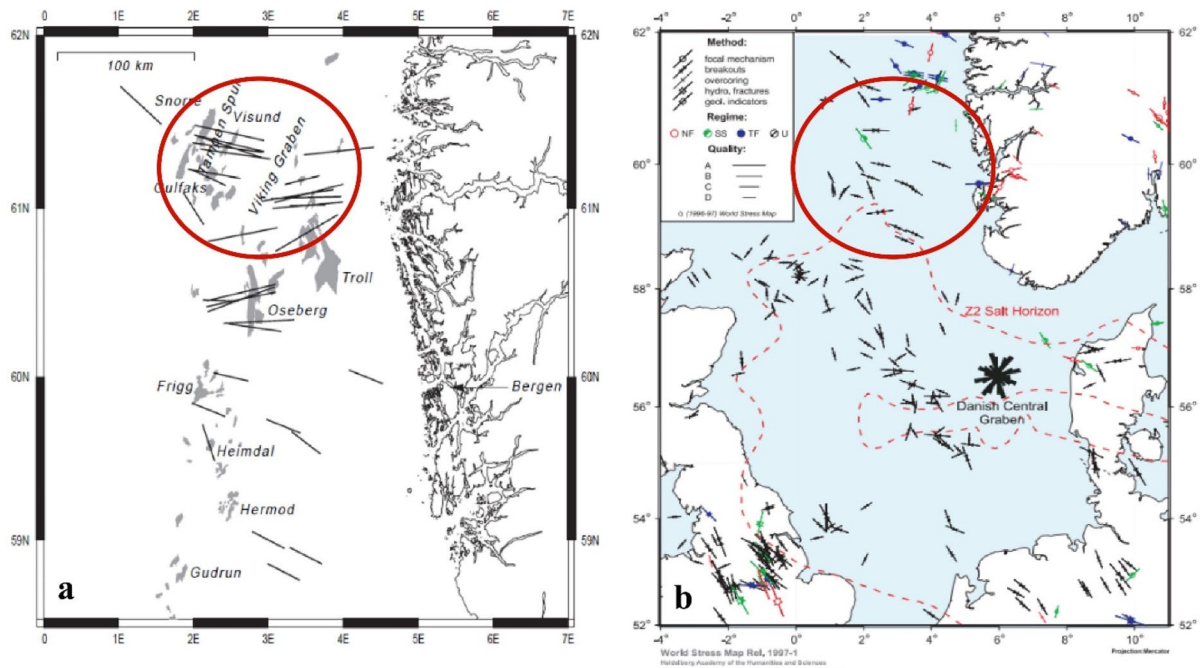


**Fig. 10** (a) Stress orientation near Viking Graben and Visund field shows roughly E-W direction of  $S_{\text{Hmax}}$  orientation (Wiprut 2001), (b) world stress map in North Sea area, the red

box indicates present study area (Hillis and Nelson 2005; Reinecker et al. 2003)

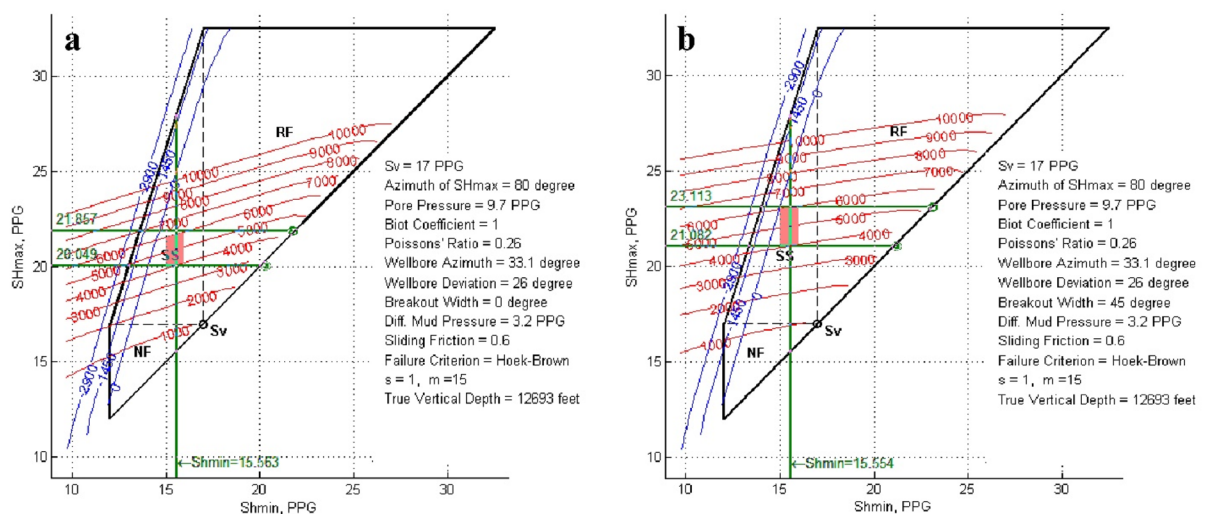


**Fig. 11** (a) Scenario-I (breakout width 0°), stress polygon analysis indicates gradient  $S_{\text{Hmax}}$  magnitude range ~20–21 ppg (~92–100 MPa), (b) scenario-II (breakout width 45°),

stress polygon analysis indicates gradient  $S_{\text{Hmax}}$  magnitude range ~21–23 ppg (~95–105 MPa)

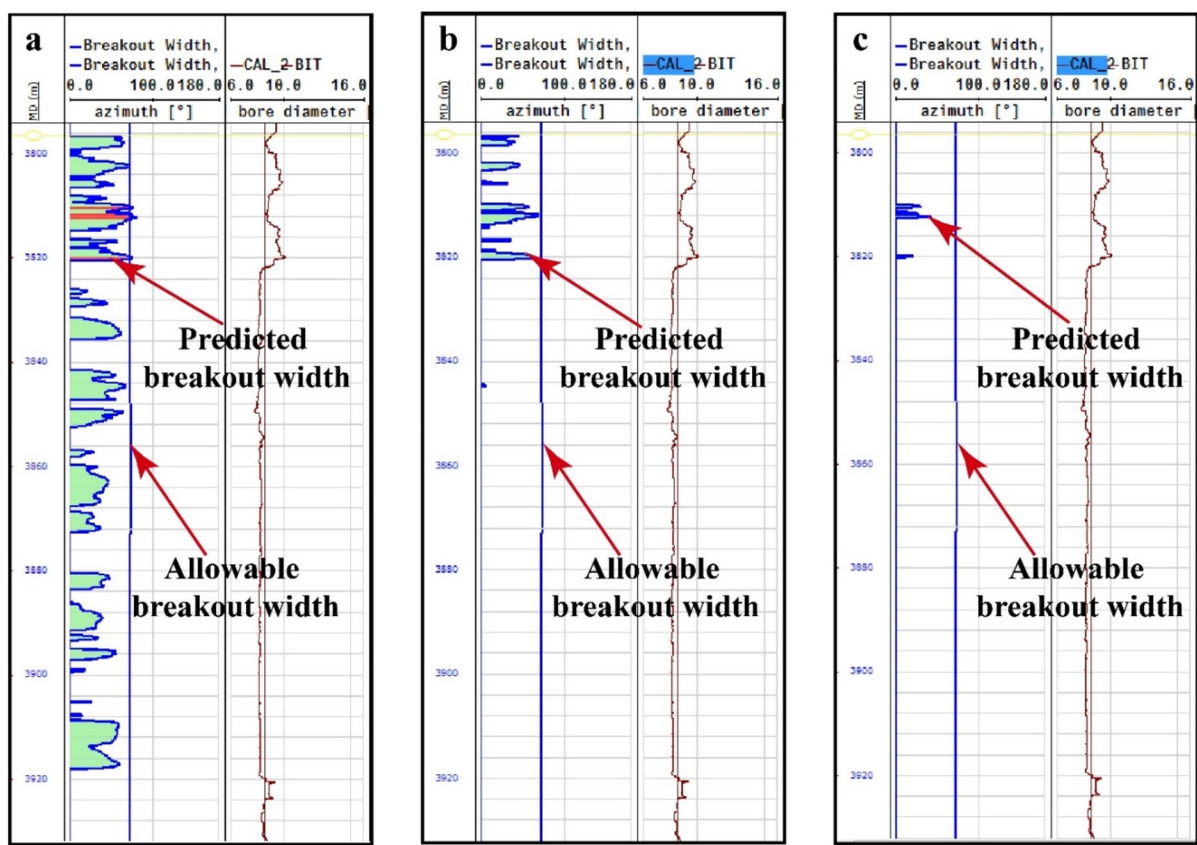


**Fig. 12** Different failure model simulation; (a) Mohr–Coulomb, (b) Hoek–Brown and (c) Modified Lade shows Hoek–Brown model is a good match with a caliper data in the third track

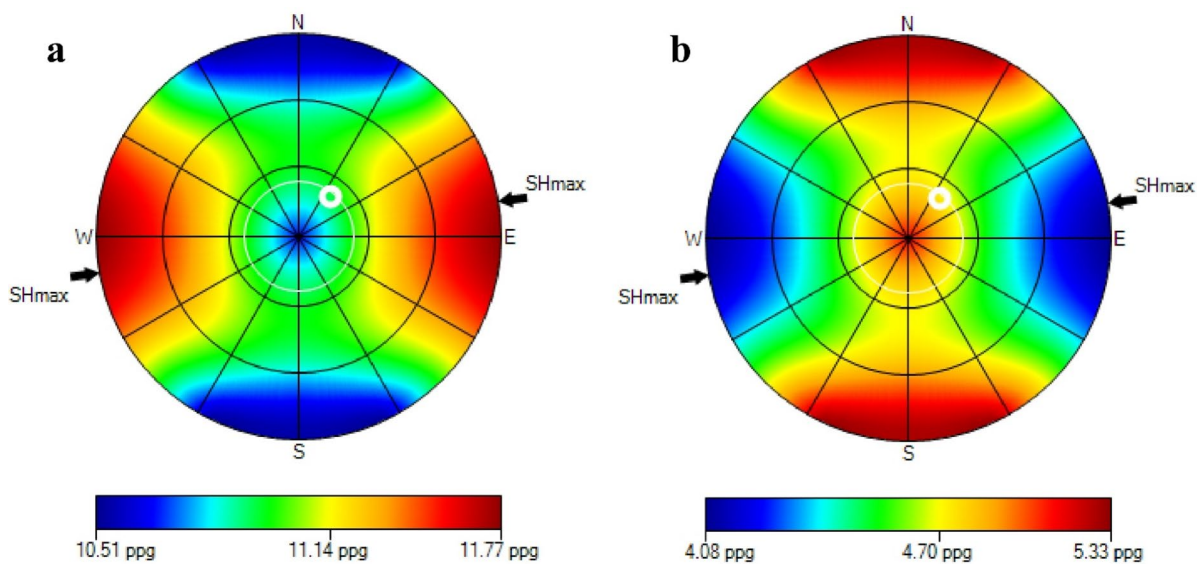


**Fig. 13** (a) Lower hemispheric stereo plot shows azimuthal and inclination sensitivity of lower bound mud weight in blue to red colour range for stable wellbore, (b) lower hemispheric

stereo plot shows azimuthal and inclination sensitivity of optimum mud weight window in blue to red colour range for safe drilling margin

**Acknowledgements** The authors would like to express their sincere gratitude to the Baker Hughes geomechanics team for their suggestions during this work.

#### Declarations

**Conflict of interest** We do not have any commercial or associative interest representing a conflict of interest with the submitted work.

#### References

- Altmann JB, Müller TM, Müller BIR, Tingay MRP, Heidbach O (2010) Poroelastic contribution to the reservoir stress path. *Int J Rock Mech Min Sci* 47:1104–1113. <https://doi.org/10.1016/j.ijrmms.2010.08.001>
- Athy LF (1930) Density, porosity, and compaction of sedimentary rocks. *Am Assoc Pet Geol Bull* 14:1–24
- Azim SA, Mukherjee P, Al-Anezi SA, Al-Otaibi B, Al-Saad B, Perumalla S, Araujo E, Babington JF (2011) Using integrated geomechanical study to resolve expensive wellbore instability problems while drilling through Zubair shale/sand sequence of Kuwait: a case study. In: Proceedings of the SPE/IADC middle east drilling technology conference and exhibition, pp. 1–14. <https://doi.org/10.2118/148049-ms>
- Baouche R, Sen S, Boutaleb K (2020) Present day In-situ stress magnitude and orientation of horizontal stress components in the eastern Illizi basin, Algeria: a geomechanical
- modeling. *J Struct Geol* 132:103975. <https://doi.org/10.1016/j.jsg.2019.103975>
- Barton N (1987) Predicting the behaviour of underground openings in jointed rock. In: 4th Manual rocha memorial lecture, Lisbon
- Barton CA, Zoback MD, Burns KL (1988) In-situ stress orientation and magnitude at the Fenton Geothermal Site, New Mexico, determined from wellbore breakouts. *Geophys Res Lett* 15:467–470. <https://doi.org/10.1029/GL015i005p00467>
- Biot MA (1941) General theory of three-dimensional consolidation. *J Appl Phys* 12:155–164
- Biot MA, Willis DG (1957) The elastic coefficients of the theory of consolidation. *J Appl Mech* 24:594–601
- Bowers GL (1995) Pore pressure estimation from velocity data: accounting for overpressure mechanisms besides undercompaction. *Soc Pet Eng SPE* 27488:89–95
- Chadwick RA, Eiken O (2013) Offshore CO<sub>2</sub> storage: Sleipner natural gas field beneath the North Sea. In: Geological storage of carbon dioxide (CO<sub>2</sub>): geoscience, technologies, environmental aspects and legal frameworks. Woodhead Publishing Limited, pp. 227–250. <https://doi.org/10.1533/9780857097279.3.227>
- Chamwudhiprecha N, Blunt MJ (2012) Carbon dioxide storage potential in the North Sea. In: International petroleum technology conference, pp. 808–821
- Eaton BA (1972) The effect of overburden stress on geopressure prediction from well logs. *J Pet Technol* 24:929–934. <https://doi.org/10.2118/3719-pa>
- Eaton BA (1975) The equation for geopressure prediction from well logs. In: Fall Meeting of the society of petroleum

- engineers of AIME. Society of Petroleum Engineers (SPE), Dallas. <https://doi.org/10.2118/5544-ms>
- Eberhardt E (2012) The Hoek–Brown failure criterion. Rock Mech Rock Eng 45:981–988. <https://doi.org/10.1007/s00603-012-0276-4>
- Ewy RT (1999) Wellbore-stability predictions by use of a modified lade criterion. SPE Drill Complet 14:85–91. <https://doi.org/10.2118/56862-PA>
- Færseth RB (1996) Interaction of Permo-Triassic and Jurassic extensional fault-blocks during the development of the northern North Sea. J Geol Soc Lond 153:931–944. <https://doi.org/10.1144/GSJGS.153.6.0931>
- Fang Z, Khaksar A (2012) Geomechanical issues and solutions for CO<sub>2</sub> sequestration in depleted hydrocarbon sandstone reservoirs. In: 46th US Rock mechanics/geomechanics symposium, pp 2286–2301
- Gale J (2004) Geological storage of CO<sub>2</sub>: what do we know, where are the gaps and what more needs to be done? Energy 29:1329–1338. <https://doi.org/10.1016/j.energy.2004.03.068>
- Gardner GHF, Gardner LW, Gregory AR (1974) Formation velocity and density - the diagnostic basics for stratigraphic traps. Geophysics 39:770–780
- GHazvinian AH, Fathi A, Moradian ZA (2008) Failure behavior of marlstone under triaxial compression. Int J Rock Mech Min Sci 45:807–814. <https://doi.org/10.1016/j.ijrmms.2007.09.006>
- Grollimund B, Zoback MD (2003) Impact of glacially induced stress changes on fault-seal integrity offshore Norway. Am Assoc Pet Geol Bull 87:493–506. <https://doi.org/10.1306/09070404063>
- Heidbach O, Tingay M, Barth A, Reinecker J, Kurfeß D, Müller B (2010) Global crustal stress pattern based on the World Stress Map database release 2008. Tectonophysics 482:3–15. <https://doi.org/10.1016/j.tecto.2009.07.023>
- Heidbach O, Rajabi M, Cui X, Fuchs K, Müller B, Reinecker J, Reiter K, Tingay M, Wenzel F, Xie F, Ziegler MO, Zoback ML, Zoback M (2018) The world stress map database release 2016: crustal stress pattern across scales. Tectonophysics 744:484–498. <https://doi.org/10.1016/j.tecto.2018.07.007>
- Hillis RR, Nelson EJ (2005) In situ stresses in the North Sea and their applications: petroleum geomechanics from exploration to development. Geol Soc Lond Pet Geo Conf Ser 6:551–564
- Hoek E, Brown ET (1980) Empirical strength criterion for rock masses. J Geotech Eng Div 106(GT9):1013–1035
- Hottman CE, Johnson RK (1965) Estimation of formation pressures from log-derived shale properties. In: SPWLA 6th annual logging symposium, society of petrophysicists and well-log analysts, Dallas
- Justwan H (2006) The petroleum systems of the South Viking Graben. University of Bergen, Norway. <https://doi.org/10.1036/13431857M106298>
- Khaksar A, Taylor PG, Fang Z, Kayes T, Salazar A, Rahman K (2009) Rock strength from core and logs: where we stand and ways to go. In: Society of petroleum engineers—EUROPEC/EAGE Conference and Exhibition, Amsterdam, pp 8–11
- Labuz JF, Zang A (2012) Mohr–Coulomb failure criterion. Rock Mech Rock Eng 45:975–979. <https://doi.org/10.1007/s00603-012-0281-7>
- Lade PV (1977) Elasto-plastic stress-strain theory for cohesionless soil with curved yield surfaces. Int J Solids Struct 13:1019–1035. [https://doi.org/10.1016/0020-7683\(77\)90073-7](https://doi.org/10.1016/0020-7683(77)90073-7)
- Nicot J (2008) Evaluation of large-scale CO<sub>2</sub> storage on freshwater sections of aquifers: an example from the Texas Gulf Coast Basin. Int J Greenh Gas Control 2:582–593. <https://doi.org/10.1016/j.ijggc.2008.03.004>
- Osagiede EE, Rotevatn A, Gawthorpe R, Kristensen TB, Jackson CAL, Marsh N (2020) Pre-existing intra-basement shear zones influence growth and geometry of non-colinear normal faults, western Utsira high-heimdal terrace. North Sea J Struct Geol 130:103908. <https://doi.org/10.1016/j.jsg.2019.103908>
- Pariseau WG (2007) Fitting failure criteria to laboratory strength tests. Int J Rock Mech Min Sci 44:637–646. <https://doi.org/10.1016/j.ijrmms.2006.09.006>
- Reinecker J, Tingay M, Müller B (2003) Borehole breakout analysis from four-arm caliper logs. World Stress Map Proj, pp 1–5
- Shukla R, Ranjith P, Haque A, Choi X (2010) A review of studies on CO<sub>2</sub> sequestration and caprock integrity. Fuel 89:2651–2664. <https://doi.org/10.1016/j.fuel.2010.05.012>
- Statoil (1993) Discovery evaluation report. Well 15/9-19SR, Theta Vest Structure-PL046A
- Tenzer R, Gladikh V (2014) Assessment of density variations of marine sediments with ocean and sediment depths. Sci World J. <https://doi.org/10.1155/2014/823296>
- Traugott M (1997) Porepressure and fracture pressure determinations in deepwater. In: Pipe line and gas industry, pp 68–70
- Vishal V (2017a) In-situ disposal of CO<sub>2</sub>: liquid and supercritical CO<sub>2</sub> permeability in coal at multiple down-hole stress conditions. J CO<sub>2</sub> Util 17:235–242. <https://doi.org/10.1016/j.jcou.2016.12.011>
- Vishal V (2017b) Saturation time dependency of liquid and supercritical CO<sub>2</sub> permeability of bituminous coals: implications for carbon storage. Fuel 192:201–207. <https://doi.org/10.1016/j.fuel.2016.12.017>
- Vishal V, Ranjith PG, Pradhan SP, Singh TN (2013a) Permeability of sub-critical carbon dioxide in naturally fractured Indian bituminous coal at a range of down-hole stress conditions. Eng Geol 167:148–156. <https://doi.org/10.1016/j.enggeo.2013.10.007>
- Vishal V, Ranjith PG, Singh TN (2013b) CO<sub>2</sub> permeability of Indian bituminous coals: implications for carbon sequestration. Int J Coal Geol 105:36–47. <https://doi.org/10.1016/j.coal.2012.11.003>
- Vishal V, Singh TN, Ranjith PG (2015) Influence of sorption time in CO<sub>2</sub>-ECBM process in Indian coals using coupled numerical simulation. Fuel 139:51–58. <https://doi.org/10.1016/j.fuel.2014.08.009>
- Vishal V, Mahanta B, Pradhan SP, Singh TN, Ranjith PG (2018) Simulation of CO<sub>2</sub> enhanced coalbed methane recovery in Jharia coalfields, India. Energy 159:1185–1194. <https://doi.org/10.1016/j.energy.2018.06.104>

- Wiprut D (2001) Stress, borehole stability and hydrocarbon leakage in the Northern North Sea. Stanford University, Stanford
- Wiprut D, Zoback M (2000) Constraining the stress tensor in the Visund feld, Norwegian North Sea Application.pdf. *Int J Rock Mech Min Sci* 37:317–336
- York P, Prichard D, Dodson J, Dodson T, Rosenberg S, Gala D, Utama B (2009) Eliminating non-productive time associated with drilling trouble zones. In: Offshore technology conference, Houston, pp 1–18. <https://doi.org/10.4043/otc-20220-ms>
- Zhang J (2011) Pore pressure prediction from well logs: methods, modifications, and new approaches. *Earth Sci Rev* 108:50–63. <https://doi.org/10.1016/j.earscirev.2011.06.001>
- Zhang J (2019) In situ stress estimate. In: Applied petroleum geomechanics, pp 187–232. <https://doi.org/10.1016/b978-0-12-814814-3.00006-x>
- Zhang J, Yin SX (2017) Fracture gradient prediction: an overview and an improved method. *Pet Sci* 14:720–730. <https://doi.org/10.1007/s12182-017-0182-1>
- Zhao J (2000) Applicability of Mohr–Coulomb and Hoek–Brown strength criteria to the dynamic strength of brittle rock. *Int J Rock Mech Min Sci* 37:1115–1121. [https://doi.org/10.1016/S1365-1609\(00\)00049-6](https://doi.org/10.1016/S1365-1609(00)00049-6)
- Zoback MD (2007) Reservoir geomechanics, reservoir geomechanics. Cambridge University Press, Cambridge. <https://doi.org/10.1017/CBO9780511586477>
- Zoback ML, Zoback MD (1989) Tectonic stress field of the continental United States. In: Pakiser LC, Mooney WD (eds) Geophysical framework of the continental United States: Boulder, Colorado, Geological Society of America Memoir 172, pp 523–539. <https://doi.org/10.1130/MEM172-p523>
- Zoback MD, Barton CA, Brady M, Castillo DA, Finkbeiner T, Grollimund BR, Moos DB, Peska P, Ward CD, Wiprut DJ (2003) Determination of stress orientation and magnitude in deep wells. *Int J Rock Mech Min Sci* 40:1049–1076. <https://doi.org/10.1016/j.ijrmms.2003.07.001>

**Publisher's Note** Springer Nature remains neutral with regard to jurisdictional claims in published maps and institutional affiliations.